JGR Space Physics

RESEARCH ARTICLE
10.1029/2020JA027782

Magnetospheric Conditions for STEVE and SAID: Particle Injection, Substorm Surge, and Field-Aligned Currents

Y. Nishimura[1], J. Yang[2], J. M. Weygand[3], W. Wang[4,2], B. Kosar[5], E. F. Donovan[6], V. Angelopoulos[3], L. J. Paxton[7], and N. Nishitani[8]

[1]Department of Electrical and Computer Engineering and Center for Space Physics, Boston University, Boston, MA, USA, [2]Department of Earth and Space Sciences, Southern University of Science and Technology, Shenzhen, China, [3]Department of Earth, Planetary and Space Sciences, University of California, Los Angeles, CA, USA, [4]School of Atmospheric Sciences, Sun Yat-sen University, Zhuhai, China, [5]Department of Physics, Catholic University of America, Washington, DC, USA, [6]Department of Physics and Astronomy, University of Calgary, Calgary, Alberta, Canada, [7]The Johns Hopkins University Applied Physics Laboratory, Laurel, MD, USA, [8]Institute for Space Earth Environmental Research, Nagoya University, Nagoya, Japan

This article is a companion to Nishimura et al. (2020), https://doi.org/10.1029/2020JA028067

Key Points:
- STEVE and SAID are associated with the substorm surge and upward currents extending more duskward than non-STEVE/SAID events
- Injection and fast plasma sheet flows also shift duskward; electron injection is stronger and ion injection is weaker
- Substorm injection extending far duskward offers a condition for STEVE and SAID due to stronger electron injection to premidnight

Supporting Information:
- Supporting Information S1
- Movie S1
- Movie S2
- Movie S3
- Movie S4

Correspondence to:
Y. Nishimura,
toshi16@bu.edu

Citation:
Nishimura, Y., Yang, J., Weygand, J. M., Wang, W., Kosar, B., Donovan, E. F., et al. (2020). Magnetospheric conditions for STEVE and SAID: Particle injection, substorm surge, and field-aligned currents. *Journal of Geophysical Research: Space Physics*, *125*, e2020JA027782. https://doi.org/10.1029/2020JA027782

Received 6 JAN 2020
Accepted 2 JUL 2020
Accepted article online 13 JUL 2020

Abstract To understand magnetosphere-ionosphere conditions that result in thermal emission velocity enhancement (STEVE) and subauroral ion drifts (SAID) during the substorm recovery phase, we present substorm aurora, particle injection, and current systems during two STEVE events. Those events are compared to substorm events with similar strength but without STEVE. We found that the substorm surge and intense upward currents for the events with STEVE reach the dusk, while those for the non-STEVE substorms are localized around midnight. The Time History of Events and Macroscale Interactions during Substorms (THEMIS) satellite observations show that location of particle injection and fast plasma sheet flows for the STEVE events also shifts duskward. Electron injection is stronger and ion injection is weaker for the STEVE events compared to the non-STEVE events. SAID are measured by Super Dual Auroral Radar Network during the STEVE events, but the non-STEVE events only showed latitudinally wide subauroral polarization streams without SAID. To interpret the observations, Rice Convection Model (RCM) simulations with injection at premidnight and midnight have been conducted. The simulations successfully explain the stronger electron injection, weaker ion injection, and formation of SAID for injection at premidnight, because injected electrons reach the premidnight inner magnetosphere and form a narrower separation between the ion and electron inner boundaries. We suggest that substorms and particle injections extending far duskward away from midnight offer a condition for creating STEVE and SAID due to stronger electron injection to premidnight. The THEMIS all-sky imager network identified the east-west length of the STEVE arc to be ~1900 km (~2.5 h magnetic local time) and the duration to be 1–1.5 h.

Plain Language Summary STEVE (strong thermal emission velocity enhancement) occurs during auroral activation called substorm, but only a small fraction of substorms come with STEVE. This study addresses what special auroral conditions are needed to create STEVE, and how the near-Earth space creates conditions for driving STEVE. We found that aurora during STEVE spreads much farther away from midnight than during non-STEVE substorms. In this situation, high-energy electrons access the near-Earth space more efficiently and drive a stronger plasma jet stream. The strong jet stream and related wave processes provide energy for driving the STEVE emission. NASA's Time History of Events and Macroscale Interactions during Substorms (THEMIS) satellites and Rice Convection Model simulations confirm the supply of high-energy electrons and the formation of the jet stream during the STEVE events.

1. Introduction

Plasma convection in the premidnight subauroral ionosphere is often enhanced at narrow (<a few degrees) latitudes, known as subauroral polarization streams (SAPS) (Foster & Burke, 2002). The latitudinal extent of the flows can occasionally become a degree or less with the peak speed exceeding a few km/s. Such narrow flows are called subauroral ion drifts (SAID) as a subset of SAPS. SAPS and SAID form as a result of magnetosphere-ionosphere feedback processes, where a latitudinally confined downward region-2 (R2)

field-aligned currents (FACs) into the subauroral ionosphere, whose conductance decreases due to fast flows (Schunk et al., 1975) and requires larger electric fields to close the current (Anderson et al., 1993). Seasonal dependence of SAID also indicates the importance of ionosphere conditions for SAID occurrence (He et al., 2014). Mishin and Puhl-Quinn (2007) suggested that particle injection and short circuiting of mesoscale plasma flows could form SAID.

While both SAPS and SAID occur during magnetically active times, notable differences can be found in terms of occurrence timings. SAPS (here we particularly refer to ones without SAID) respond almost immediately to substorms (Mishin & Mishin, 2007; Nishimura et al., 2008; Zou & Nishitani, 2014). In contrast, SAID are more often found during the substorm recovery phase (Anderson et al., 1993; Makarevich et al., 2011), although SAID could also occur during the expansion phase (Mishin, 2016). The timing difference between SAPS and SAID indicates that the magnetospheric state during SAID is quite different from SAPS and brings up interesting questions about what is the magnetospheric driver(s) of SAID, and how different those magnetospheric conditions are compared to SAPS. Even when SAPS and SAID occur at the same time, SAID are located closer to midnight and SAPS are found duskward of SAID (Anderson et al., 2001). Although a number of SAPS simulation studies have reproduced basic properties of SAPS (e.g., Ferdousi et al., 2019; Yu et al., 2015), it has been challenging to simulate SAID due to difficulties in accurately specifying localized magnetospheric drivers. Particle injection has been considered to initiate SAID (Buzulukova et al., 2010; Wei et al., 2019; Zhang et al., 2009). However, it is not understood what nature of particle injection distinguishes SAPS and SAID. This calls for a detailed observation and modeling study of magnetosphere conditions for driving SAID.

Recently, the strong thermal emission velocity enhancement (STEVE) has been found to be a subauroral optical feature associated with SAID with larger magnitudes than average SAID (Archer et al., 2019; MacDonald et al., 2018). Since plasma flow measurements are often limited in space and time, the optical signature can be useful for finding when and where intense SAID exist. Nishimura et al. (2019) showed that STEVE corresponds to SAID, waves, and ion and electron injection boundaries nearly collocated with each other in the inner magnetosphere. Since STEVE occurs during the substorm recovery phase (Gallardo-Lacourt et al., 2018), substorm injection from the magnetotail is likely the energy source. However, STEVE is much less common than substorms (Gallardo-Lacourt et al., 2018), indicating that only a certain type of substorms possesses conditions for STEVE's occurrence. Revealing such conditions would contribute to understand how intense SAID forms.

The purpose of the present study is to examine magnetospheric conditions for STEVE and intense SAID during the substorm recovery phase. Specifically, we investigate substorms with and without STEVE and examine differences in auroral structures, particle injection, and currents. We show that large duskward expansion of the substorm activity and injection provides stronger electron injection and SAID than for non-STEVE substorms.

The Time History of Events and Macroscale Interactions during Substorms (THEMIS) all-sky imager (ASI) network in North America is used to detect STEVE and auroral structures in the auroral oval. Defense Meteorological Satellite Program (DMSP) Special Sensor Ultraviolet Spectrographic Imager (SSUSI) data also assists to find the spatial extent of substorm aurora. The THEMIS satellites in the magnetotail measure plasma sheet particles and electromagnetic fields. The Super Dual Auroral Radar Network (SuperDARN) radars identify SAPS and SAID. The spherical elementary currents systems (SECS) method provides vertical currents derived from the divergence of the curl-free system from the network of ground magnetometers as a proxy of FACs (Weygand & Wing, 2016; Weygand et al., 2011). We selected two STEVE events with the THEMIS satellites in the nightside plasma sheet. Two other events with similar magnetic conditions and satellite locations but without STEVE were selected for examining differences in auroral and plasma sheet conditions between the STEVE and non-STEVE events. The Rice Convection Model-Equilibrium (RCM-E) simulation model (Toffoletto et al., 2003; Yang et al., 2011) is used to interpret observation results. A companion paper by Nishimura et al. (2020) presents low-altitude satellite measurements and discusses evolution of particle boundaries in the topside ionosphere for events with and without STEVE. The present paper pays attention to magnetosphere and auroral signatures.

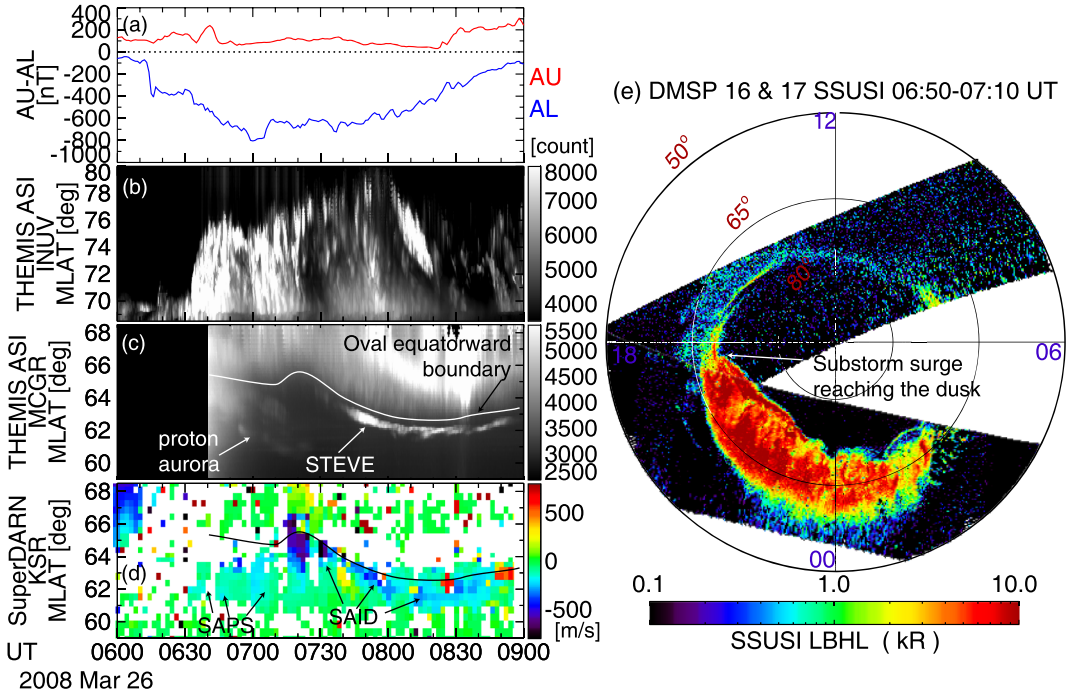

Figure 1. A substorm event on 26 March 2008. (a) *AU* and *AL* indices, THEMIS ASI keograms at (b) Inuvik (INUV) and (c) McGrath (MCGR, turned on at 6:40 UT), (d) SuperDARN line-of-sight velocity data at King Salmon (KSR), and (e) SSUSI Lyman-Birge-Hopfield long (LBHL, 165–180 nm) data from DMSP 16 and 17 at 6:50–7:20 UT. DMSP 17 was in the Southern Hemisphere. See Figure 2 for the THEMIS ASI locations.

2. Results

2.1. The 26 March 2008 Event With STEVE

Figures 1–3 present a satellite-ground conjunction event of STEVE on 26 March 2008. Low-altitude satellite data of this event are studied in Nishimura et al. (2020). The expansion phase of a substorm started at ~6:10 UT (Figure 1a) and the peak *AL* index was −800 nT. Figures 1b–1c present THEMIS ASI keograms at 20–21 magnetic local time (MLT) in Alaska, where STEVE was detected. The subauroral ionosphere showed diffuse aurora during the expansion phase at 06:15–07:00 UT (proton aurora; see Nishimura et al., 2020), and then a STEVE arc appeared during the recovery phase between ~07:22 and ~09:00 UT (Figure 1c). Colored photographs by a citizen scientist during this event show a mauve-colored STEVE arc equatorward of green diffuse aurora (http://www.spaceweather.com/aurora/gallery_01mar08_page4.htm). The STEVE arc was preceded by a large auroral brightening in the poleward portion of the auroral oval in Alaska starting at ~06:30 and rebrightening at ~07:00 UT (Figure 1b), and a rapid equatorward shift of the equatorward boundary of the auroral oval (Figure 1c). The SuperDARN line-of-sight (LOS) velocity data in the STEVE region show a latitudinally narrow (~1°) and enhanced velocity during the recovery phase (Figure 1d), whose flow speed and latitudinal motion are correlated with STEVE arc's luminosity and latitudinal motion. In Figure S5a in the supporting information, the LOS velocity is converted to the westward flow assuming that the LOS velocity is a projection of the westward flow. It clearly shows that the westward velocity exceeds 1 km/s in a narrow (~1°) latitude range measured by full-width half-maximum during the recovery phase, satisfying the Foster and Burke (2002) definition of SAID. During the expansion phase, there was no persistent narrow and fast flow peak. Nishimura et al. (2020) showed using two radars and DMSP conjunctions that this is a SAID flow channel. In the DMSP SSUSI data at 6:50–7:20 UT (Figure 1e), the substorm auroral bulge extended to ~18.5 MLT, and the substorm active aurora filled the dusk-midnight sector.

Figure 2 shows selected snapshots of the THEMIS ASI data and vertical currents using the SECS method. Prior to the substorm (Figure 2a), the currents in the premidnight sector were weak and showed a typical large-scale upward region-1 (R1) and downward region-2 (R2) pattern. During the expansion phase

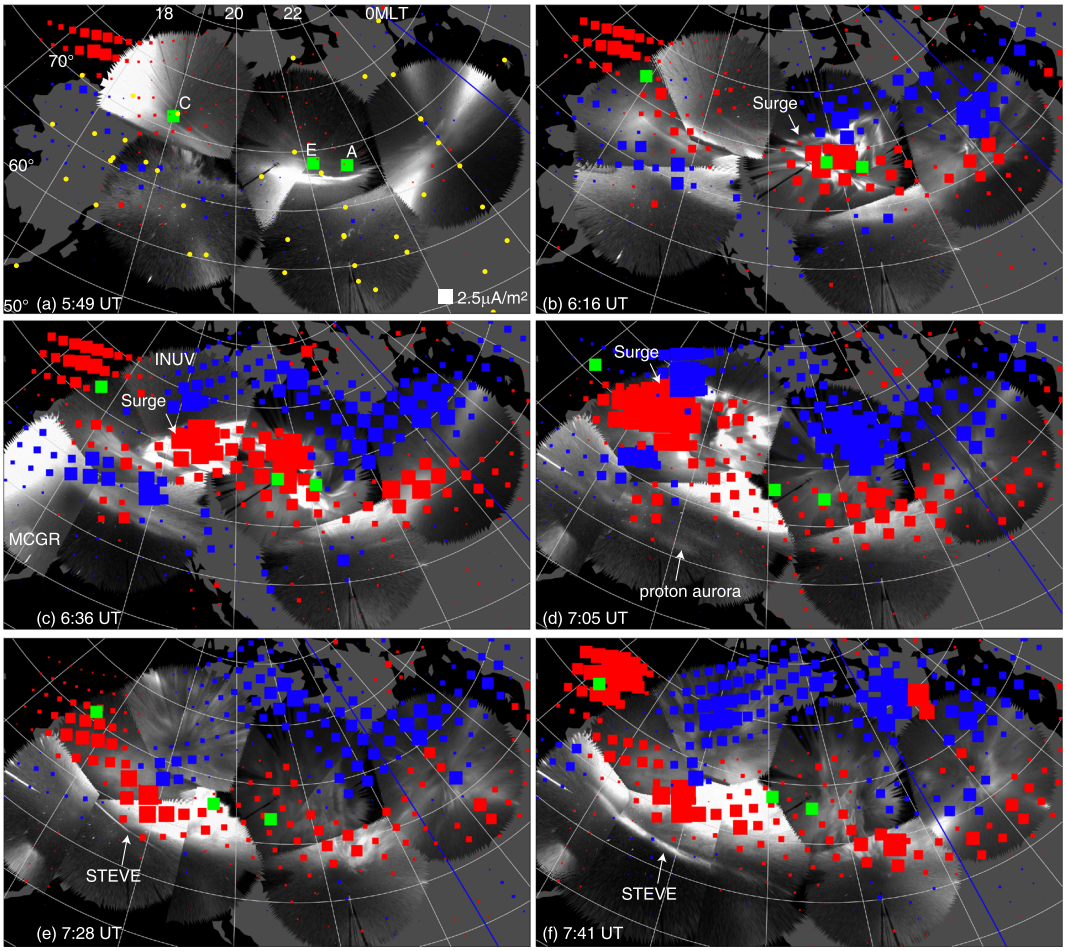

Figure 2. Selected THEMIS ASI snapshots mapped to the sky at 110 km height for the Figure 1 event. The red and blue dots overlaid on the imager data show vertical upward and downward currents using the SECS method. The size of the dots indicates the strength of the currents (scaled to the 2.5 uA/m2 reference size shown at the bottom right corner). The magnetic footprints of the THEMIS satellites using the T01 model (Tsyganenko, 2002) are marked in green. Locations of the ground magnetometers are marked by yellow dots in Figure 2. The blue line marks the magnetic midnight. The whole sequence of the ASI and SECS data is given in Movie S1.

(Figures 2b–2d), most intense upward currents were located over the surge. The surge was initially located near midnight (22 MLT) and then propagated to 20 MLT within 30 min. The surge then left the imager coverage and reached at least 18.5 MLT (Figure 1d). Proton aurora was the only notable emission at subauroral latitudes during the expansion phase (see Polar Operational Environmental Satellites [POES]-17 data shown in Figure 3 of Nishimura et al., 2020). In the early recovery phase at 07:00–07:20 UT, the surge and streamers reactivated (Figure 2d) and the auroral equatorward boundary moved equatorward, while the subauroral proton aurora faded away. Then the STEVE arc appeared just equatorward of the auroral oval (Figure 2e) within the longitude range where the surge and streamers were present. The entire extent of the STEVE arc was covered by three imagers (Figure 2f), and the arc extended over 2.5 h MLT length (1,950 km). Then the STEVE arc disappeared near the end of the substorm (~1.5 h duration). The R2 currents near the equatorward boundary of the auroral oval at premidnight were downward during the early expansion phase (Figures 2b and 2c) and then turned upward during the late expansion (>21 MLT, Figure 2d) and recovery (>19 MLT, Figures 2e–2f) phases. Here we pay attention to upward currents over diffuse aurora near the oval equatorward boundary and do not include the upward current over the surge. The currents in the poleward portion of the auroral oval also changed from upward to downward after the passage of the surge and streamers. Morphologically, the premidnight region appears to be connected to the postmidnight current system (downward R1 and upward R2) during the late

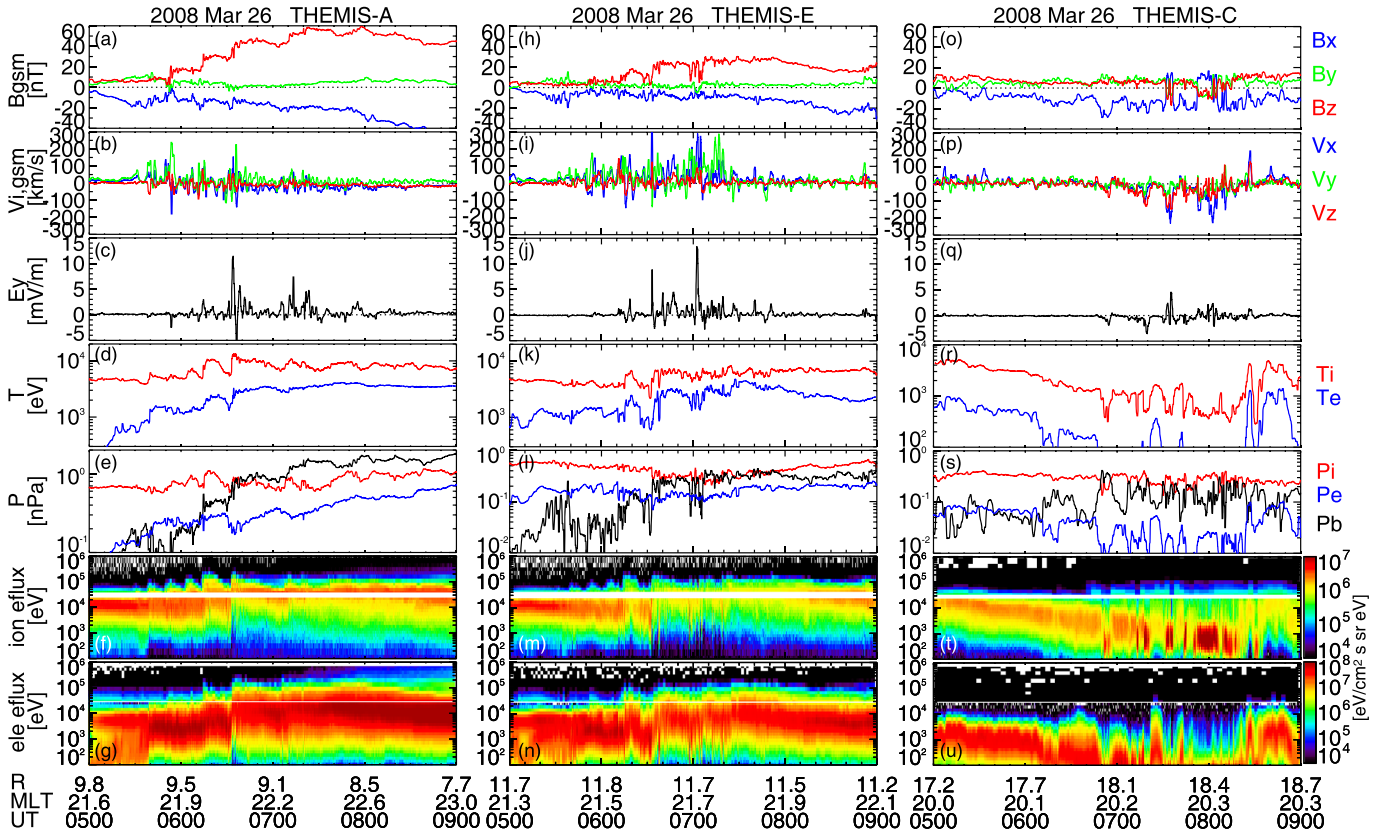

Figure 3. THEMIS-A, E, and C data during the Figure 1 event. From top to bottom, each column shows the magnetic field, ion velocity perpendicular to the magnetic field, pressure (red: ion thermal pressure, blue: electron thermal pressure, black: magnetic pressure), ion energy flux, and electron energy flux. THEMIS is located at premidnight.

expansion and recovery phases. This premidnight current distribution is drastically different from typical FAC distributions at premidnight during substorms and enhanced geomagnetic activity, where currents at premidnight are upward in R1 and downward in R2 (Anderson et al., 2018; Korth et al., 2011).

Figure 3 shows in situ data from THEMIS-A, E, and C. All satellites detected a series of dipolarizations, fast flows, and particle flux enhancements but with time delays: ~06:05–07:20 UT at THEMIS-A at ~22 MLT, ~06:10–07:23 UT at THEMIS-E at ~21.7 MLT, and ~06:50–08:30 UT at THEMIS-C at ~20.3 MLT. THEMIS-C detected tailward flows and thus was located tailward of the reconnection region. The plasma β (the ratio between the thermal and magnetic pressures in the fifth panels) during the fast flows was close to 1, indicating that the satellites were in the central plasma sheet. Despite being at premidnight, THEMIS-A and E measured notable dispersionless electron injection at each dipolarization, where an arbitrary reference level of flux (10^6 [eV/cm^2 s sr eV]) was found up to 100 keV. The electron energy flux during the injections peaked at ~10 keV on average. The electron temperature was ~3 keV, and the ratio between the ion and electron temperatures (T_i/T_e) was ~2 during the fast flows. The ratio between the ion and electron pressures (P_i/P_e) during the fast flows was ~2.3. The temperature and pressure occasionally went down during the substorm expansion phase, but those were seen outside the dipolarizations and fast flows. Our focus is on plasma being injected to the inner magnetosphere during the fast flows.

2.2. March 11, 2008 Event Without STEVE

We compare the properties of the STEVE event in section 2.1 to those of a substorm event without STEVE shown in Figure 4. The Figure 4 substorm event has a strength (AL ~ −600 nT), onset time (05:55 UT), and onset location (22 MLT) that are comparable to the section 2.1 event. In addition, this event occurred in the same year and month (March 2008) and a similar level of the presubstorm magnetic activity ($|AL| < 100$ nT). However, no optical emission was found equatorward of the auroral oval (Figures 4c and 4e), and subauroral flows had more than 1° of latitudinal extent (Figure 4d), that is, SAPS without SAID.

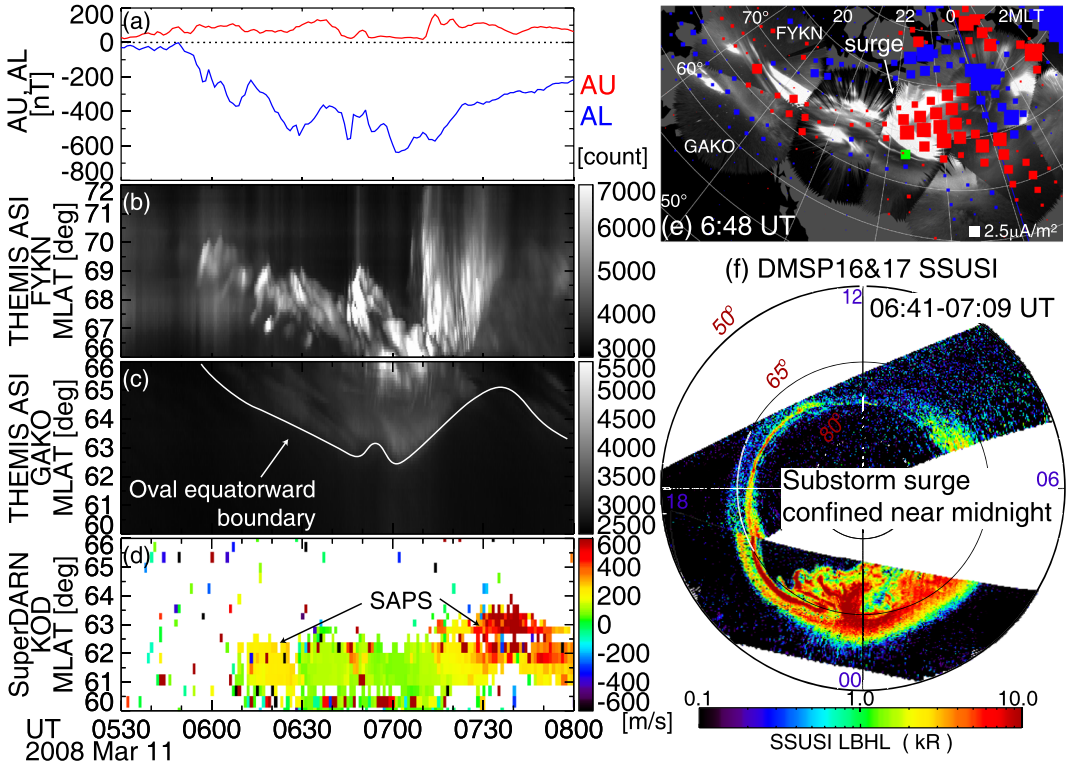

Figure 4. A substorm event on 11 March 2008 without STEVE. (a) *AU* and *AL*, imager keograms at (b) Fort Yukon (FYKN) and (c) GAKO, (d) SuperDARN velocity, (e) imager data snapshot and SECS currents at 6:48 UT, and (e) DMSP SSUSI LBHL data at 6:40–7:10 UT. The whole sequence of the ASI and SECS data is given in Movie S2.

See also Figure S5b. These events offer a good opportunity to find conditions that differentiate STEVE/SAID and non-STEVE/SAPS events.

Figure 4e shows a snapshot of aurora and currents 1 h after the substorm onset near the end of the expansion phase. In contrast to Figure 2, the most intense aurora (expansion-phase surge and streamers) and upward currents stayed close to the onset MLT (22 MLT). This is not due to the limited coverage of the THEMIS ASIs, but the DMSP SSUSI imaging (Figure 4f) also shows that the substorm surge was much more localized than in Figure 1d. Movie S2 and Figure 4b show that an auroral brightening was eventually seen over Alaska at 7:11 UT, but it only lasted for ~10 min and did not have a significant impact to the SECS currents, in contrast to the Figure 2 case, where the intense surge and associated currents reached Alaska when the *AL* index was nearly at the peak value. Rather, the *AL* index shows that it was in the substorm recovery phase, where the currents were overall decaying in time. We consider that it was a weak brightening in the recovery phase rather than an intense surge propagating to Alaska. The premidnight R2 currents were mostly directed downward, consistent with typical premidnight FACs during active times (Anderson et al., 2018; Korth et al., 2011).

THEMIS-D was located in the central plasma sheet ($\beta > 3$) and close to the location of THEMIS-E in the section 2.1 event (Figures 5a–5g, 11.8 R_E and 22.4 MLT during the fast flows). THEMIS-C was nearly at the same MLT and detected similar features further downtail. Both satellites detected a series of dipolarizations, fast flows, and particle injections at 5:30–7:00 UT, as typical signatures of a substorm. However, a notable difference from the previous event is the strength of the electron injection. Comparing THEMIS-D in this event and THEMIS-E in Figure 3, the electron temperature in Figure 5d was lower ($T_e = 2$ keV on average during the injections), and the 10^6 [eV/cm^2 s sr eV] flux only reached ~30 keV on average. The ion energy flux and energy were larger ($T_i = 10$ keV, $T_i/T_e = 5$, $P_i/P_e = 4$) than in the section 2.1 event, indicating that the non-STEVE substorm event was dominated by ion injection, while the STEVE event had a larger contribution of electron injection. In addition, the dawn-dusk electric field was weaker than in the previous event (Figures 3c and 5c).

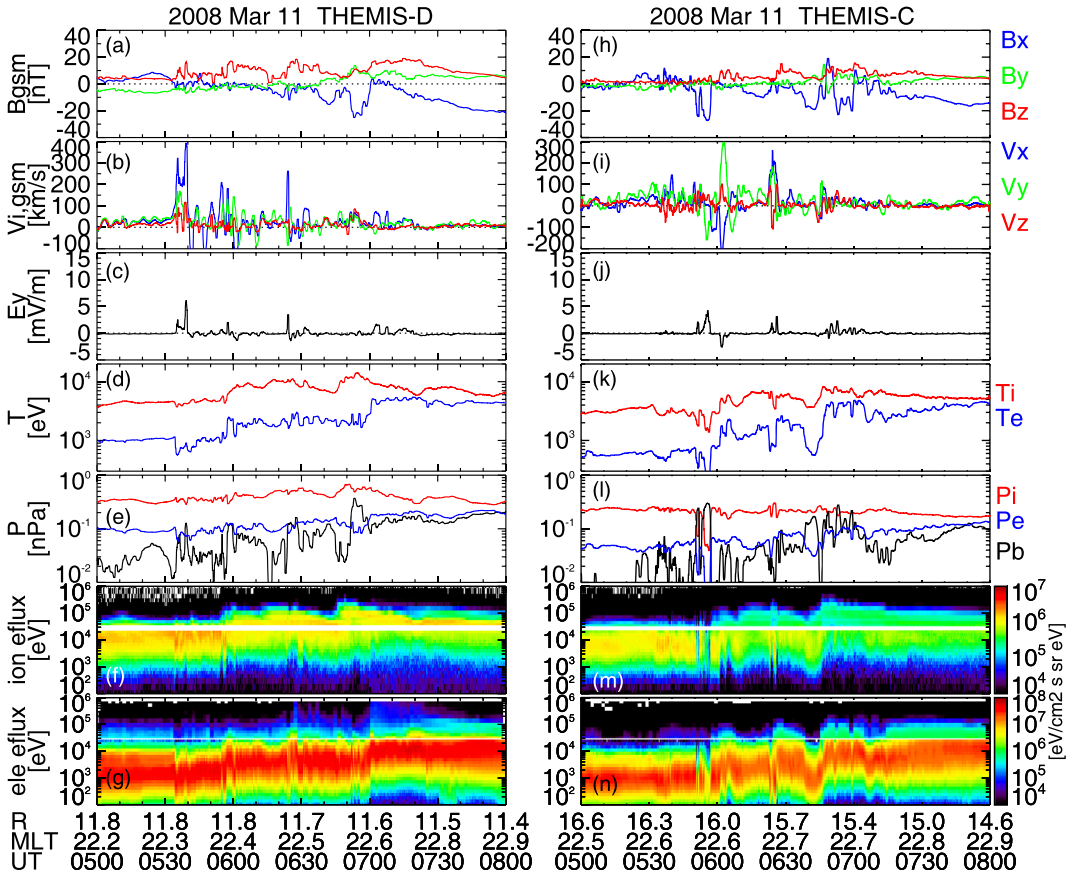

Figure 5. THEMIS-D and C satellite data for the Figure 4 event. The format is the same as in Figure 3. THEMIS-D and C are located at premidnight.

2.3. The 5 April 2010 Event With STEVE

We use another pair of events with and without STEVE (Figures 6 and 7), where the THEMIS satellites were located at midnight. Figure 6 summarizes the space-ground observations of the 5 April 2010 STEVE event. This event shows similar features to the section 2.1 event. This substorm had a peak *AL* of −550 nT, and the STEVE arc occurred at 05:30–06:30 UT, soon after a large auroral brightening and equatorward shift of the equatorward boundary of the auroral oval near the end of the expansion phase (Figures 5b and 5c). SAID flows of ~1° latitudinal extent occurred when STEVE was present (see also Figure S5c). The arc extended over 2.5 h MLT length (1,900 km). The largest upward currents during STEVE were found at 19 MLT, and much of the premidnight R2 currents was directed upward. The DMSP SSUSI data show that the substorm surge reached 18 MLT and the substorm bulge spanned the entire dusk-midnight sector. This STEVE arc was not detected in the SSUSI data likely because the latitudinal extent of the arc (15 km) was smaller than the SSUSI spatial resolution (~20 km).

THEMIS-A was located near midnight with $\beta \sim 1$ (Figure 8). Similar to the Figure 3 event, the 10^6 [eV/cm^2 s sr eV] flux was found up to ~100 keV on average, while T_i/T_e was ~1, and P_i/P_e was ~2. The dipolarizations were gradual, indicating that the satellite is away from the injection region, which is consistent with the auroral measurements that the surge is located far duskward.

2.4. February 1, 2008 Event Without STEVE

The STEVE event in section 2.3 is compared to a substorm event without STEVE, shown in Figure 7. Both events had THEMIS in the plasma sheet near midnight at a similar radial distance and a magnetically quiet precondition ($|AL| < 100$ nT). The Figure 6 substorm event was weaker ($AL \sim -300$ nT) and thus magnitudes cannot be compared, but we only compare the morphology of the measured properties. There was no STEVE emission in the subauroral ionosphere (Figure 7c). Movie S4 shows a diffuse emission at 6:15–6:40 UT, but it

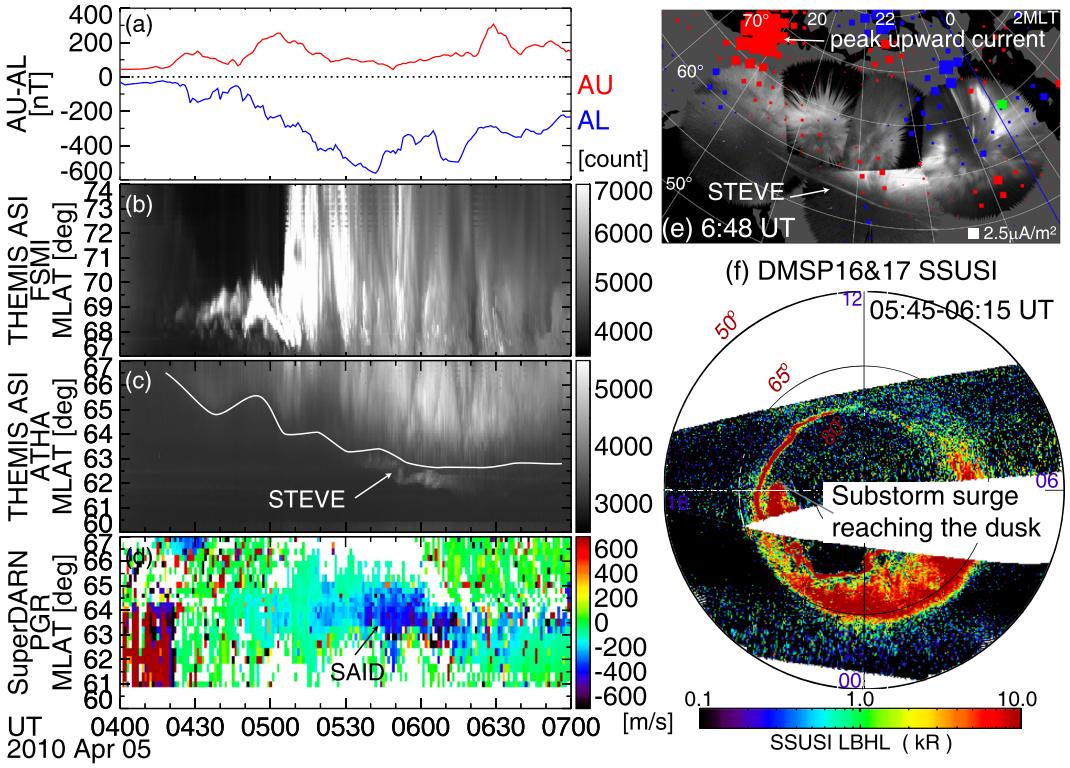

Figure 6. A substorm event on 5 April 2010 with STEVE between 5:30 and 6:30 UT. The format is the same as in Figure 4. The whole sequence of the ASI and SECS data is given in Movie S3.

is proton aurora with temporal intensity modulation associated with Pc1 pulsation (Figure S7) (Nomura et al., 2016). The subauroral flows spread over >3° latitude and thus those are SAPS flows without SAID (Figures 7d and S5d). The largest upward currents were seen at midnight, and the premidnight currents showed an upward R1 and downward R2 structure. The surge only reached ~21 MLT (Figures 7e and 7f).

THEMIS-D was located near midnight in the central plasma sheet ($\beta \sim 2$) and detected a sharp dipolarization front and fast flow, indicating that the satellite was in the injection region. It is consistent with the auroral measurements that the surge was located near midnight. Comparing to the THEMIS measurements in the section 2.3 event, the injection location in this event is located closer to midnight. The 10^6 [eV/cm^2 s sr eV] flux was found only up to 50 keV on average. On the other hand, the ion flux and energy were higher than in the previous event. These differences can also be seen as a higher T_i/T_e (~3) and P_i/P_e (~3). The temperature difference suggests that THEMIS-A in the section 2.3 event was located dawnward of the injection location and measured electrons drifting away from the injection region.

2.5. RCM Simulation

A comparison of the four conjunction events above indicates notable differences between the STEVE and non-STEVE substorm events. The STEVE events are associated with a substorm surge and upward currents extending to the dusk, and SAID flows. The duskward extension of the substorm activity corresponds to duskward propagation of magnetotail reconnection and particle injection locations, and contributions of electron injection are larger. In the non-STEVE events, the substorm auroral activity is more localized around midnight, subauroral flows are wider in latitude (SAPS without SAID), and contributions of ion injection are larger. These results indicate that the duskward shift of injection could be related to the SAID occurrence and collocation of the ion and electron injection boundaries seen in the event studied by Nishimura et al. (2019).

To quantify the role of the duskward shift of the injection location in SAID and injection boundaries, we conducted two RCM-E simulation runs. The model setup follows the previous RCM-E simulations by Yang

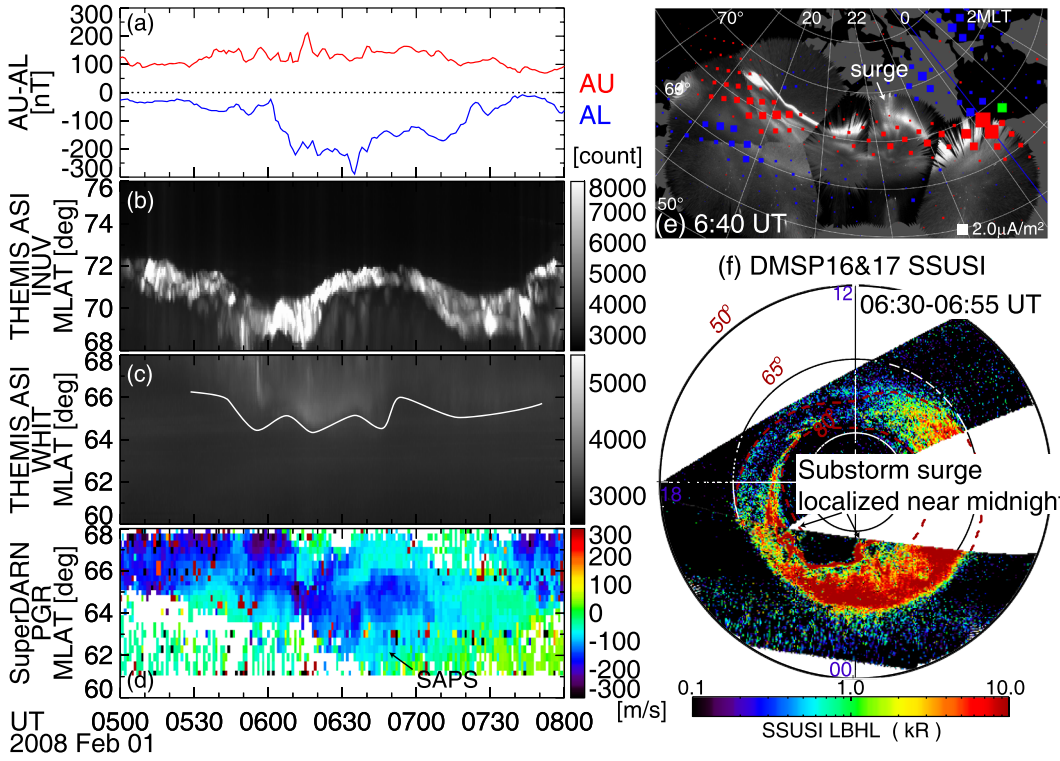

Figure 7. A substorm event on 1 February 2008 without STEVE. The format is the same as in Figure 4. The whole sequence of the ASI and SECS data is given in Movie S4.

et al. (2011, 2012, 2014). The outer boundary near midnight is at 15 R_E. The ionospheric conductance is obtained by the sum of the International Reference Ionosphere-90 empirical ionospheric model and enhancement due to plasma sheet electron precipitation (Chen & Schulz, 2001). The initial equilibrium condition is obtained by steady convection with a 30 kV polar cap potential drop until $t = 0$. After $t = 0$, bubbles are injected three times (at $t = 0$, 10, and 20 min) at the outer boundary at 23 MLT (Run 1) and 21 MLT (Run 2). For each bubble, the flux tube entropy parameter $PV^{5/3}$ at the outer boundary is reduced to 50% of the value prior to the bubble injection for 5 min. The width of the bubbles is 0.5 h MLT. For other times and locations, the boundary conditions are set the same as during the steady convection interval.

Figures 9a–9c show results for the bubble injections at 23 MLT (Run 1), 4 min after the first bubble was injected through the outer boundary. A reduced entropy channel can be found at 23 MLT (Figure 9a), and the enhanced electric field characterizes the fast flow channel (Figures 9b and 9c). The background ion hot plasma density (constituting the ring current) was located at ~6–8 R_E peaking at midnight. At premidnight, the earthward boundary of the electron hot plasma density (electron plasma sheet) was located tailward of the ion earthward boundary. SAPS flows were found at ~19–21 MLT and 6.6–8 R_E.

After the bubble injections at $t = 35$ min (Figures 9d–9f), the ion earthward boundary at 19–22 MLT was found more earthward due to the injections and subsequent duskward drifts, while the electron earthward boundary at >22 MLT shifted earthward due to the injections and dawnward drifts. The SAPS electric field intensified (i.e., denser potential contours), but the radial width of the electric field stayed essentially the same. Because most of the injected electrons did not reach the premidnight sector, the injected electrons did not substantially affect SAPS in this simulation run.

In simulation Run 2 with bubbles injected at 21 MLT (Figures 9g–9l), the electrons were injected to the premidnight sector and they were found to significantly affect SAPS. The ions at 21 MLT were injected slightly earthward and were confined around 6 R_E, while the electrons were injected earthward more substantially due to the enhanced electric field in the flow channel. As a result, the earthward boundaries of the ions and electrons at 20–21 MLT were nearly collocated. The SAPS electric field in this region became confined to the

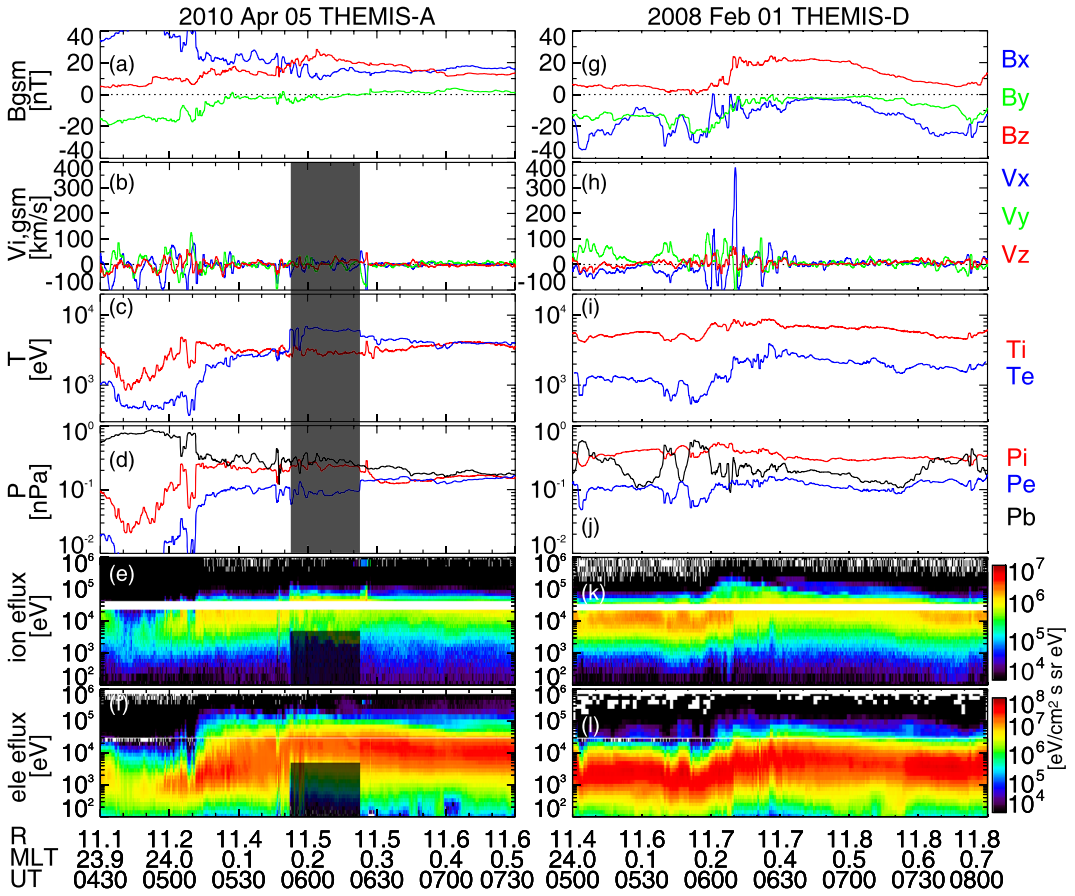

Figure 8. THEMIS satellite data for the Figures 6 and 7 events. The format is the same as in Figure 3 except that the electric field data are not shown due to satellite charging. The THEMIS satellites are located near midnight. THEMIS-A was in Earth's shadow during the shaded time interval and is not used.

narrow (~0.5 R_E width) region between the earthward boundaries of ions and electrons. The ~0.5 R_E width around the geosynchronous orbit maps to ~1° latitude width, and thus this is the SAID electric field. The SAPS region has shifted further to the dusk. The narrower width of flow from dusk to premidnight is consistent with SAID observations (Anderson et al., 2001).

Figure S6 compares simulated FACs in the ionosphere for the two RCM-E runs at $t = 35$ min. In simulation Run 2, the R2 FACs below 65° MLAT have shifted duskward by ~1 MLT (down to ~21 MLT as opposed to ~22 MLT for Run 1). This is consistent with the observation that more upward R2 FACs were seen in the premidnight sector for the SAID/STEVE events.

The comparison between the two simulation runs suggests that, when the particle injection region shifts duskward, more electrons access the premidnight sector and reduce the L-shell separation of the earthward boundaries of ions and electrons. The SAPS electric field is confined to the narrow separation of the particle boundaries because the region between the equatorward boundaries of the R2 FACs (ion earthward boundary) and electron precipitation (electron earthward boundary) also becomes narrow. The reduced width of the particle boundaries due to premidnight electron injections could be the condition for creating SAID by shrinking the L-shell (or latitude in the ionosphere) extent of the SAPS. The narrow width of the particle boundaries and the confinement of the SAID electric field between the particle boundaries are consistent with the in situ observations (Nishimura et al., 2019) and low-altitude satellite observations (Nishimura et al., 2020). The duskward shift of the injection location also explains the duskward extension of the upward R2 FACs. In this simulation, we injected only three bubbles for simplicity, but in reality more injections occur over a longer time period during a substorm. Thus, the simulated structures seen at $t = 35$ min would not be a transient but longer-lasting structures.

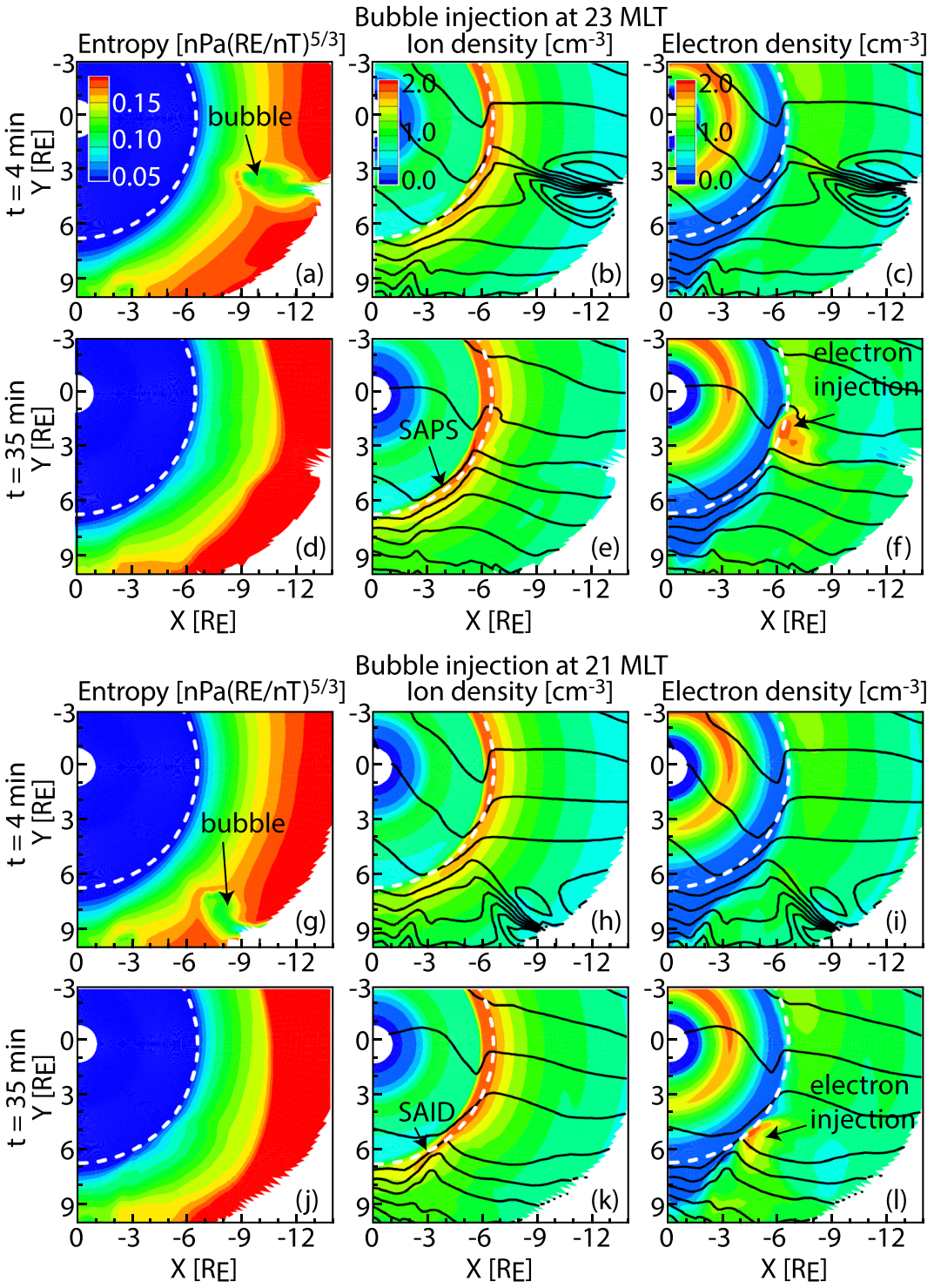

Figure 9. RCM simulation results with a bubble injection (a–f) at 23 MLT and (g–l) at 21 MLT. (left) Flux tube entropy ($PV^{5/3}$), (middle) ion number density, and (right) electron number density. (a–c and g–i) During the first bubble injection (t = 4 min), and (d–f and j–l) after three bubble injections (t = 35 min). The black lines show equipotential contours every 1.5 kV. The white dashed circle marks the geosynchronous orbit.

3. Conclusion

We examined magnetosphere-ionosphere conditions that are associated with STEVE and SAID during the substorm recovery phase, by comparing substorms with and without STEVE. We found that the substorms with STEVE and SAID are characterized by the substorm surge and upward currents propagating to the dusk, resulting in the substorm auroral activity that extends over the entire dusk-midnight sector. Substorm injection location also shifts duskward, and injection near midnight has larger contributions by electrons. Upward R2 FACs also extends duskward. For the substorms without STEVE, SAID were absent, the substorm auroral activity was localized near midnight, and injection near midnight was more dominated by ions. The RCM-E simulations showed that injection at premidnight brought more electrons to the pre-midnight inner magnetosphere and shrunk the separation between the earthward boundaries of electrons and ions at premidnight. The SAPS electric field became narrower at premidnight (SAID) and was confined between the narrow separation of the particle boundaries, and the wide SAPS region has shifted to the dusk-side. On the other hand, injection at midnight intensified SAPS but did not change the flow radial width. These results indicate that the duskward shift of magnetotail reconnection region controls the occurrence of STEVE and SAID. The multiple THEMIS ASIs also showed that the east-west length of the STEVE arc is ~1,900 km (~2.5 h MLT) and the duration is 1–1.5 h.

Acknowledgments

This work was supported by NASA Grants NNX17AL22G and 80NSSC18K0657, National Science Foundation Grants AGS-1737823 and AGS-1907698, and AFOSR Grant FA9559-16-1-0364. The THEMIS mission and all-sky imagers are supported by NASA Contract NAS5-02099, Canadian Space Agency Contract 9F007-046101, and National Science Foundation Grant AGS-1004736. The THEMIS, DMSP, and SuperDARN data were obtained through themis.ssl.berkeley.edu, cdaweb.gsfc.nasa.gov, cedar.openmadrigal.org and vt.superdarn.org. The RCM output can be accessed through https://doi.org/10.5281/zenodo.3460651. Data access and processing used SPEDAS V3.1 (Angelopoulos et al., 2019).

References

Anderson, B. J., Olson, C. N., Korth, H., Barnes, R. J., Waters, C. L., & Vines, S. K. (2018). Temporal and spatial development of global Birkeland currents. *Journal of Geophysical Research: Space Physics*, *123*, 4785–4808. https://doi.org/10.1029/2018JA025254

Anderson, P. C., Carpenter, D. L., Tsuruda, K., Mukai, T., & Rich, F. J. (2001). Multisatellite observations of rapid subauroral ion drifts (SAID). *Journal of Geophysical Research*, *106*, 29,585–29,599. https://doi.org/10.1029/2001JA000128

Anderson, P. C., Hanson, W. B., Heelis, R. A., Craven, J. D., Baker, D. N., & Frank, L. A. (1993). A proposed production model of rapid subauroral ion drifts and their relationship to substorm evolution. *Journal of Geophysical Research*, *98*(A4), 6069–6078. https://doi.org/10.1029/92JA01975

Angelopoulos, V., Cruce, P., Drozdov, A., Grimes, E. W., Hatzigeorgiu, N., King, D. A., et al. (2019). *Space Science Reviews*, *215*(1), 9. https://doi.org/10.1007/s11214-018-0576-4

Archer, W. E., Gallardo-Lacourt, B., Perry, G. W., St-Maurice, J.-P., Buchert, S. C., & Donovan, E. F. (2019). Steve: The optical signature of intense subauroral ion drifts. *Geophysical Research Letters*, *46*, 6279–6286. https://doi.org/10.1029/2019GL082687

Buzulukova, N., Fok, M.-C., Pulkkinen, A., Kuznetsova, M., Moore, T. E., Glocer, A., et al. (2010). Dynamics of ring current and electric fields in the inner magnetosphere during disturbed periods: CRCM–BATS-R-US coupled model. *Journal of Geophysical Research*, *115*, A05210. https://doi.org/10.1029/2009JA014621

Chen, M. W., & Schulz, M. (2001). Simulations of storm time diffuse aurora with plasmasheet electrons in strong pitch angle diffusion. *Journal of Geophysical Research*, *106*(A2), 1873–1886. https://doi.org/10.1029/2000JA000161

Ferdousi, B., Nishimura, Y., Maruyama, N., & Lyons, L. R. (2019). Subauroral neutral wind driving and its feedback to SAPS during the 17 March 2013 geomagnetic storm. *Journal of Geophysical Research: Space Physics*, *124*, 2323–2337. https://doi.org/10.1029/2018JA026193

Foster, J. C., & Burke, W. J. (2002). SAPS: A new categorization for sub-auroral electric fields. *Eos Transactions AGU*, *83*(36), 393–394. https://doi.org/10.1029/2002EO000289

Gallardo-Lacourt, B., Nishimura, Y., Donovan, E., Gillies, D. M., Perry, G. W., Archer, W. E., et al. (2018). A statistical analysis of STEVE. *Journal of Geophysical Research: Space Physics*, *123*, 9893–9905. https://doi.org/10.1029/2018JA025368

He, F., Zhang, X.-X., & Chen, B. (2014). Solar cycle, seasonal, and diurnal variations of subauroral ion drifts: Statistical results. *Journal of Geophysical Research: Space Physics*, *119*, 5076–5086. https://doi.org/10.1002/2014JA019807

Korth, H., Rastätter, L., Anderson, B. J., & Ridley, A. J. (2011). Comparison of the observed dependence of large-scale Birkeland currents on solar wind parameters with that obtained from global simulations. *Annales Geophysicae*, *29*(10), 1809–1826. https://doi.org/10.5194/angeo-29-1809-2011

MacDonald, E. A., Donovan, E. F., Nishimura, Y., Case, N. A., Gillies, D. M., Gallardo-Lacourt, B., et al. (2018). New science in plain sight: Citizen scientists lead to discovery of optical structure in the upper atmosphere. *Science Advances*, *3*, eaaq0030. https://doi.org/10.1126/sciadv.aaq0030

Makarevich, R. A., Kellerman, A. C., Devlin, J. C., Ye, H., Lyons, L. R., & Nishimura, Y. (2011). SAPS intensification during substorm recovery: A multi-instrument case study. *Journal of Geophysical Research*, *116*, A11311. https://doi.org/10.1029/2011JA016916

Mishin, E. V., & Mishin, V. (2007). Prompt response of SAPS to stormtime substorms. *Journal of Atmospheric and Solar-Terrestrial Physics*, *69*(10–11), 1233–1240. https://doi.org/10.1016/j.jastp.2006.09.009

Mishin, E. V. (2016). SAPS onset timing during substorms and the westward traveling surge. *Geophysical Research Letters*, *43*, 6687–6693. https://doi.org/10.1002/2016GL069693

Mishin, E. V., & Puhl-Quinn, P. A. (2007). SAID: Plasmaspheric short circuit of substorm injections. *Geophysical Research Letters*, *34*, L24101. https://doi.org/10.1029/2007GL031925

Nishimura, Y., Donovan, E. F., Angelopoulos, V., & Nishitani, N. (2020). Dynamics of auroral precipitation boundaries associated with STEVE and SAID. *Journal of Geophysical Research: Space Physics*, *125*, e2020JA028067. https://doi.org/10.1029/2020JA028067

Nishimura, Y., Gallardo-Lacourt, B., Zou, Y., Mishin, E., Knudsen, D. J., Donovan, E. F., et al. (2019). Magnetospheric signatures of STEVE: Implications for the magnetospheric energy source and interhemispheric conjugacy. *Geophysical Research Letters*, *46*, 5637–5644. https://doi.org/10.1029/2019GL082460

Nishimura, Y., Wygant, J., Ono, T., Iizima, M., Kumamoto, A., Brautigam, D., & Friedel, R. (2008). SAPS measurements around the magnetic equator by CRRES. *Geophysical Research Letters*, *35*, L10104. https://doi.org/10.1029/2008GL033970

Nomura, R., Shiokawa, K., Omura, Y., Ebihara, Y., Miyoshi, Y., Sakaguchi, K., et al. (2016). Pulsating proton aurora caused by rising tone Pc1 waves. *Journal of Geophysical Research: Space Physics*, *121*, 1608–1618. https://doi.org/10.1002/2015JA021681

Schunk, R. W., Raitt, W. J., & Banks, P. M. (1975). Effect of electric fields on the daytime high-latitude E and F regions. *Journal of Geophysical Research*, *80*(22), 3121–3130. https://doi.org/10.1029/JA080i022p03121

Toffoletto, F. R., Sazykin, S., Spiro, R. W., & Wolf, R. A. (2003). Inner magnetospheric modeling with the Rice convection model. *Space Science Reviews*, *107*(1/2), 175–196. https://doi.org/10.1023/A:1025532008047

Tsyganenko, N. A. (2002). A model of the near magnetosphere with a dawn-dusk asymmetry: 1. Mathematical structure. *Journal of Geophysical Research*, *107*(A8), 1179. https://doi.org/10.1029/2001JA000219

Wei, D., Yu, Y., & He, F. (2019). The magnetospheric driving source of double-peak subauroral ion drifts: Double ring current pressure peaks. *Geophysical Research Letters*, *46*, 7079–7087. https://doi.org/10.1029/2019GL083186

Weygand, J., & Wing, S. (2016). Comparison of DMSP and SECS region-1 and region-2 ionospheric current boundary. *Journal of Atmospheric and Solar-Terrestrial Physics*, *143*, 8–13.

Weygand, J. M., Amm, O., Viljanen, A., Angelopoulos, V., Murr, D., Engebretson, M. J., et al. (2011). Application and validation of the spherical elementary currents systems technique for deriving ionospheric equivalent currents with the North American and Greenland ground magnetometer arrays. *Journal of Geophysical Research*, *116*, A03305. https://doi.org/10.1029/2010JA016177

Yang, J., Toffoletto, F. R., & Wolf, R. A. (2014). RCM-E simulation of a thin arc preceded by a north-south-aligned auroral streamer. *Geophysical Research Letters*, *41*, 2695–2701. https://doi.org/10.1002/2014GL059840

Yang, J., Toffoletto, F. R., Wolf, R. A., & Sazykin, S. (2011). RCM-E simulation of ion acceleration during an idealized plasma sheet bubble injection. *Journal of Geophysical Research*, *116*, A05207. https://doi.org/10.1029/2010JA016346

Yang, J., Toffoletto, F. R., Xing, X., & Angelopoulos, V. (2012). RCM-E simulation of the 13 March 2009 steady magnetospheric convection event. *Journal of Geophysical Research*, *117*, A03224. https://doi.org/10.1029/2011JA017245

Yu, Y., Jordanova, V., Zou, S., Heelis, R., Ruohoniemi, M., & Wygant, J. (2015). Modeling subauroral polarization streams during the 17 March 2013 storm. *Journal of Geophysical Research: Space Physics*, *120*, 1738–1750. https://doi.org/10.1002/2014JA020371

Zhang, J.-C., Wolf, R. A., Spiro, R. W., Erickson, G. M., Sazykin, S., Toffoletto, F. R., & Yang, J. (2009). Rice convection model simulation of the substorm-associated injection of an observed plasma bubble into the inner magnetosphere: 2. Simulation results. *Journal of Geophysical Research*, *114*, A08219. https://doi.org/10.1029/2009JA014131

Zou, Y., & Nishitani, N. (2014). Study of mid-latitude ionospheric convection during quiet and disturbed periods using the SuperDARN Hokkaido radar. *Advances in Space Research*, *54*(3), 473–480. https://doi.org/10.1016/j.asr.2014.01.011